



# Cathodoluminescence microscopy: Optical imaging and spectroscopy with deep-subwavelength resolution

Toon Coenen, Benjamin J.M. Brenny, Ernst Jan Vesseur, and  
Albert Polman

*The following article is based on the Innovation in Materials Characterization Award presentation given by Albert Polman at the 2014 Materials Research Society Spring Meeting in San Francisco. Polman was recognized "For the development, application, and commercialization of Angle-Resolved Cathodoluminescence Imaging Spectroscopy as a new tool for optical imaging at the nanoscale, with applications in nanophotonics and materials science in general."*

This article describes a new microscope, based on angle-resolved cathodoluminescence (CL) imaging spectroscopy, which enables optical imaging and spectroscopy at deep-subwavelength spatial resolution. We used a free electron beam in a scanning electron microscope as a direct excitation source for polarizable materials, and we collected the emitted coherent visible/infrared CL radiation using a specially designed optical collection system that is integrated in the electron microscope. We have demonstrated the use of this new technique for the excitation of plasmons in single metal nanoparticles, surface plasmon polaritons at metal surfaces, resonant Mie modes in dielectric nanostructures, and cavity modes and Bloch modes in photonic crystals. Using angle-resolved detection, we are able to derive the nature of localized modes and the dispersion of propagation modes in dielectric and plasmonic geometries. An outlook about new directions and applications of CL imaging spectroscopy is also provided.

## Introduction

With the growing importance of nanotechnology, the demand for high-resolution microscopy and characterization techniques has tremendously increased. Conventional optical microscopy is limited in resolution by the diffraction limit for light, making it unsuitable for optical studies at the nanoscale. Near-field optical microscopy,<sup>1</sup> in which a nanoscale tip scans over a surface to collect radiation, provides higher spatial resolution but is experimentally complex and often suffers from unavoidable interaction between the tip and the analyzed surface. Other advanced microscopy techniques, such as stimulated emission depletion microscopy,<sup>2</sup> photoactivated localization microscopy,<sup>3</sup> and stochastic optical reconstruction microscopy,<sup>4</sup> show sub-wavelength resolution but require the use of fluorescent labels. A label-free optical imaging technique with deep-subwavelength resolution, which has recently gained significant

interest, is based on the use of a focused beam of fast electrons as an optical excitation source. As electrons can be focused to nanoscale dimensions, this technique yields deep-subwavelength optical resolution.

An electron beam is a very pure optical excitation source. The time-varying evanescent electric field around the electron trajectory can interact with a polarizable medium, resulting in elemental optical materials excitations. These excitations can be probed by studying the energy loss of the electrons (electron energy loss spectroscopy) or by detecting the optical radiation that is subsequently emitted by the material (cathodoluminescence, CL).<sup>5</sup> The spatial resolution of excitation is determined by the electron beam spot size, which is on the order of 1 nm, as well as the radial extent of the evanescent electric field about the electron beam, which is on the order of 10 nm, depending on the beam energy. The spectral extent of

Toon Coenen, Center for Nanophotonics, FOM Institute AMOLF, The Netherlands  
Benjamin J.M. Brenny, Center for Nanophotonics, FOM Institute AMOLF, The Netherlands  
Ernst Jan Vesseur, Center for Nanophotonics, FOM Institute AMOLF, The Netherlands  
Albert Polman, Center for Nanophotonics, FOM Institute AMOLF, The Netherlands; polman@amolf.nl  
DOI: 10.1557/mrs.2015.64

excitation is determined by the interaction time of the electron with the sample, which is typically less than one femtosecond. This is less than one optical cycle of the emitted radiation and corresponds to a broad spectral range, making the moving electron a broadband optical excitation source spanning the ultraviolet/visible/infrared spectral range.

Electron beams can also excite materials by impact excitation or through secondary electrons generated inside the material. This incoherent CL emission has been known for decades and is used in the study of optically active semiconductors, quantum dots, lanthanide ions, and radiative point defects in materials.<sup>6</sup> As the secondary electron cloud is much larger in size than the primary electron beam, the spatial resolution of incoherent CL imaging is usually poor, except when confocal light collection techniques are used,<sup>7</sup> in which case the resolution is limited by the diffraction limit.

This article focuses on the coherent excitation method offered by electron-beam excitation in which the electron beam is used as a direct excitation source for characteristic materials resonances in nanostructured optical materials. This excitation mechanism can usually be purely described by electrodynamics and requires knowledge of only the electron-beam energy, material geometry, and materials optical constants.<sup>1,8</sup> In this article, we review a new microscope we designed and built to utilize this deep-subwavelength excitation method, and we highlight the fundamental nanophotonics insights we gained.

## Cathodoluminescence imaging instrument

The main component of the new CL imaging instrument is a 30 keV scanning electron microscope (SEM, FEI XL-30) equipped with a Schottky field emission gun (see **Figure 1a**). This electron source provides the nA beam currents required to obtain sufficient CL signal. The SEM is equipped with a specially designed micromanipulation stage, which carries an off-axis aluminum paraboloid mirror with a  $1.46\pi$  sr acceptance angle (**Figure 1b–c**). The electron beam reaches the sample through a 600- $\mu\text{m}$ -diameter hole in the paraboloid, directly above its focal point. The mirror collects the generated CL and redirects it out of the SEM through a glass vacuum flange into an enclosed optics box (black box in **Figure 1a**). The micromanipulation stage allows for proper focusing of the paraboloid by using four piezoelectric stepper motors connected to a titanium leaf spring system (visible in **Figure 1b**). This system provides translational degrees of freedom ( $x, y$ ) as well as control over mirror tilt and yaw. Vertical alignment of the sample with mirror focus is achieved by varying the SEM stage height. Achieving precise alignment of the parabola's focus and beam path with the nanostructure

under investigation is essential to collecting reproducible and well-calibrated CL data.

**Figure 1d** shows a schematic of the CL setup. For spectral imaging purposes, the CL that is collected by the paraboloid is focused onto a multimode fiber using an achromatic lens. The fiber is connected to one of two spectrometers, with either a liquid-nitrogen-cooled silicon charge-coupled device (CCD) array (sensitivity wavelength range  $\lambda = 400\text{--}900$  nm) or a liquid-nitrogen-cooled InGaAs photodiode array ( $\lambda = 900\text{--}1650$  nm). In CL imaging mode, the electron beam is raster scanned over the surface and a spectrum is taken at every beam position. In this way, a three-dimensional CL intensity datacube with  $x$ -position/ $y$ -position/wavelength coordinates is collected. A typical two-dimensional (2D) spatial scan composed of  $50 \times 50$  pixels in the  $x$  and  $y$  directions is taken in 10 minutes. To avoid the effect of beam drift during CL measurements, SEM images are recorded regularly during the measurements and the measurement area is adjusted if needed. CL imaging is a powerful correlative technique in which SEM and CL images can be directly overlaid and compared.

A second important feature of the CL instrument is its capability to measure the angular distribution of the emitted radiation.<sup>9,10</sup> The 2D lateral intensity profile of the parallel beam emanating from the paraboloid mirror is a direct measure of the angular emission distribution. We measure the beam profile by directing it to a 2D Peltier-cooled back-illuminated  $1024 \times 1024$  pixel CCD array. A schematic illustration of this

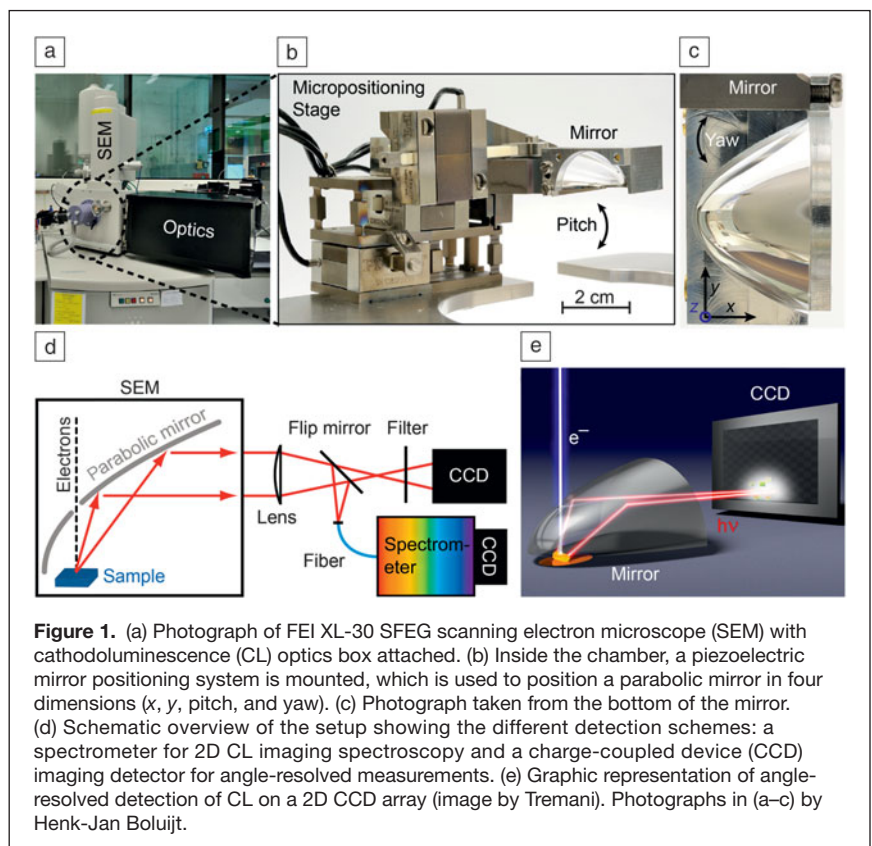


**Figure 1.** (a) Photograph of FEI XL-30 SFE scanning electron microscope (SEM) with cathodoluminescence (CL) optics box attached. (b) Inside the chamber, a piezoelectric mirror positioning system is mounted, which is used to position a parabolic mirror in four dimensions ( $x, y$ , pitch, and yaw). (c) Photograph taken from the bottom of the mirror. (d) Schematic overview of the setup showing the different detection schemes: a spectrometer for 2D CL imaging spectroscopy and a charge-coupled device (CCD) imaging detector for angle-resolved measurements. (e) Graphic representation of angle-resolved detection of CL on a 2D CCD array (image by Tremani). Photographs in (a–c) by Henk-Jan Boluijt.

type of measurement is shown in Figure 1e. The achromatic lens is defocused to ensure that the beam fills the entire CCD array. This collection geometry is similar to Fourier imaging (also known as conoscopic imaging or defocused imaging) in microscopy: The wave vector distribution of emitted light is directly imaged onto the CCD. If the mirror is well-focused, each point in the CCD image corresponds to light reflected off a single point on the paraboloid and corresponds to a unique emission angle described by a zenithal angle  $\theta$  running from  $0^\circ$  to  $90^\circ$  (where  $\theta = 0^\circ$  is normal to the surface) and an azimuthal angle  $\varphi$  running from  $0^\circ$  to  $360^\circ$  (where the paraboloid vertex is at  $\varphi = 180^\circ$ ). Using the proper coordinate transform, the data collected on the CCD are converted to units of emitted power per steradian.

To obtain spectral selectivity in this angle-resolved measuring mode, 40-nm-bandpass color filters are used. A typical wavelength-filtered angular measurement at a single beam position is taken in 30 seconds. In a second geometry, a pinhole is placed in the optical beam path and scanned in a plane normal to the emitted beam while the collected radiation is analyzed using a spectrometer. Angle- and spectral-resolved data can thus be taken at the same time. Such measurements provide higher spectral resolution but at the expense of a longer measuring time. Other optical components such as polarizers and retarders can also be introduced in the optical beam path.

## Results

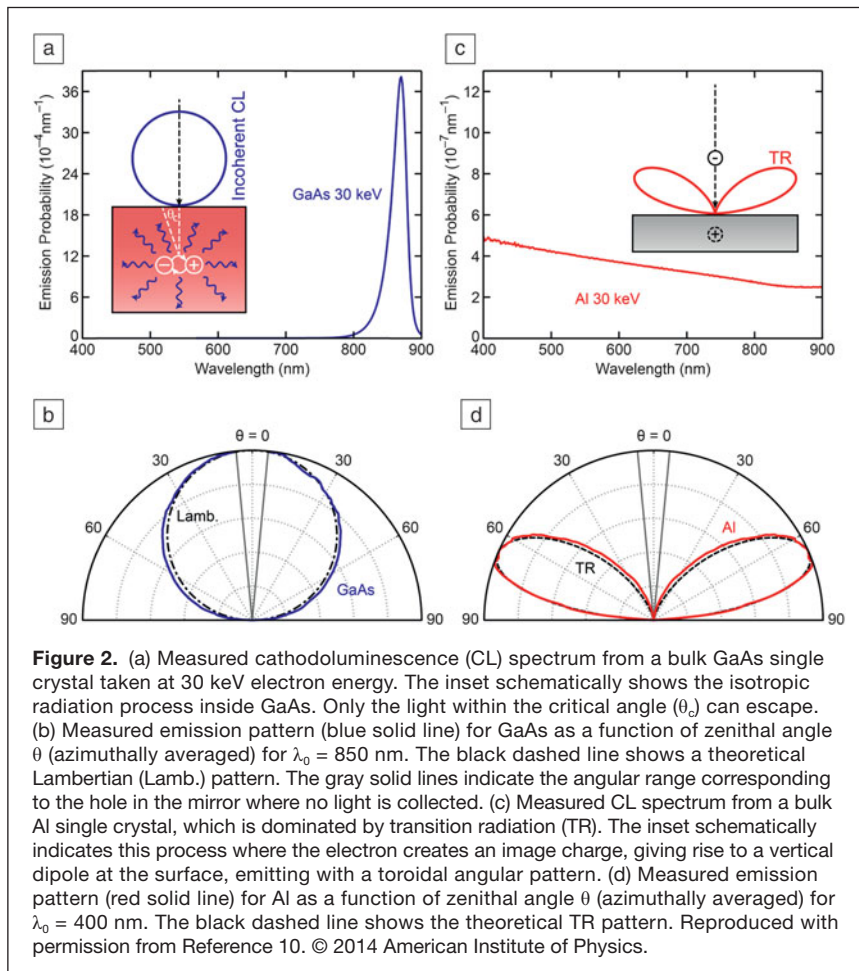
### Incoherent versus coherent emission

Figure 2a shows a CL spectrum taken from a bulk gallium arsenide crystal measured using our CL setup showing the characteristic band-edge emission at  $\lambda_0 = 870$  nm.<sup>11</sup> The measured azimuthally-averaged angular emission distribution around  $\lambda_0 = 870$  nm is shown in Figure 2b. A Lambertian angular profile is found, consistent with an isotropic emission distribution within the GaAs crystal (see inset in Figure 2a). The emission observed here is the “classical” incoherent CL observed in many systems before. Angular measurements of incoherent CL can find applications in characterization of optoelectronic devices such as light-emitting diodes (LEDs) and solar cells.

We studied the coherent emission that occurs when the incident electron beam passes through the vacuum/material interface. Figure 2c shows this transition radiation (TR) spectrum for a polished surface of an aluminum single crystal.<sup>10</sup> A broad featureless spectrum is observed over the entire spectral range collected by the detector ( $\lambda_0 = 400$ –900 nm). This TR spectrum can be explained to first order by a simple electrodynamic model, in which the electron approaching the interface induces an image charge in

the metal, thus inducing an effective vertical dipole moment that is oriented upward. This transient dipole then decays into the far field with a characteristic doughnut emission pattern. The observed CL spectrum reflects the inherent broad spectral nature of the electron-beam-induced excitation process as discussed above. The vertical scales in Figure 2a and c indicate the absolute emission rates per incident photon, per unit bandwidth. When integrated over the spectral range shown in Figure 2c, the TR emission rate is about  $2 \times 10^{-4}$  photons per incident electron.

The measured angular emission pattern at  $\lambda_0 = 400$  nm is shown in Figure 2d together with a calculation of the TR radiation pattern;<sup>5</sup> very good agreement between the two distributions is observed. The spectrum and angular profile of TR are only determined by the electron-beam energy and the optical constants of the substrate. Note that aluminum, like most metals, does not exhibit efficient intraband optical transitions and hence the spectrum in Figure 2c–d is dominated by TR. We note that a TR band is also present in the spectrum for GaAs in Figure 2a. However, it is overshadowed by the  $\sim 5000$  times stronger incoherent band gap emission. As TR is a well-characterized phenomenon, and metals show only weak incoherent emission, we use the combination of TR



measurements and calculations for either single-crystal Al or Ag to calibrate the CL system, so that absolute CL measurements can be performed on other samples.

### Excitation of plasmonic nanoparticles

We investigated the electron-beam-induced generation of nanoscale optical resonators next. The left inset in **Figure 3a** shows a SEM image of a single Au nanodisk on a Si substrate, made using electron-beam lithography and liftoff techniques. The Au nanoparticle is 100 nm in diameter and has a height of 80 nm. **Figure 3a** shows a CL spectrum obtained by spatially averaging the CL emission collected from a raster scan over the particle with 5 nm resolution. A clear resonant spectrum is observed, which reflects the radiation of a vertically-oriented dipolar plasmon resonance in the Au nanoparticle, peaking at  $\lambda_0 = 560$  nm. Plasmons are elementary excitations of free electrons in metals. They can be efficiently excited as the electric field of the electron beam passing through the nanoparticle can couple to the unbound charges. The linewidth of the resonant peak in the spectrum is determined by radiative and Ohmic damping. A spatial map of CL emission in **Figure 3a** shows the nanoparticle plasmon is excited for all beam positions, but most efficiently in the center, where the electron beam direction aligns with the plasmonic eigenmode's vertical dipole moment. Plasmonic metal nanoparticles and particle networks can find applications as antennas; for example, to enhance spontaneous emission,<sup>12</sup> form building blocks in sub-wavelength optical integrated circuits,<sup>13</sup> create optical hot spots for sensing,<sup>14</sup> enhance light absorption in photodetectors<sup>15</sup> and thin-film solar cells,<sup>16</sup> as well as applications in photothermal therapy<sup>17</sup> and transparent conducting nanowire meshes.<sup>18,19</sup>

The angular distribution of the radiation emitted by the single Au nanoparticle is shown in **Figure 3b**, in which the electron

beam was placed on the left edge of the nanoparticle (see cartoon on the right in **Figure 3b**).<sup>20</sup> The CL emission intensity is shown as a function of zenithal angle  $\theta$  and azimuthal angle  $\phi$ . The black region around  $\phi = 0^\circ$ , where no light is observed, corresponds to the opening in the paraboloid mirror (see **Figure 1b–c**). While the nanoparticle excited at its center (data not shown) shows a symmetric angular profile reflecting the doughnut-type emission from an upward-pointing dipole, in this case the measured angular distribution shows a clear left-right asymmetry. CL emission is more intense toward the right side of the angular pattern (around  $\phi = 90^\circ$ ) than toward the left side (around  $\phi = 270^\circ$ ). This asymmetry arises from the fact that off-center excitation with the electron beam leads to the simultaneous excitation of in-plane and out-of-plane dipole components which interfere in the far-field.<sup>20</sup> This nanoscale beaming effect co-rotates with the electron-beam excitation position (data not shown). A more detailed analysis of the far-field interference of dipolar electric and magnetic dipole modes as well as quadrupolar modes is given in References 21 and 22.

### Excitation of surface plasmon polaritons

Because the electron-beam-induced excitation is localized, it represents a large range of optical wave vectors. This, together with the inherently broad excitation spectrum, allows direct excitation of surface plasmon polaritons (SPPs). These guided surface waves have in-plane momenta larger than that of free-space light at the same frequency and cannot be directly excited with light. SPPs are transverse-magnetic waves, with their electric field pointing in the normal direction, and thus, couple well with the incident electron beam. In a simple model, the point dipole composed of the incident electron and its image charge in the metal decays, according to Fermi's Golden Rule, to the available modes, in this case both the far field (TR) and SPPs.

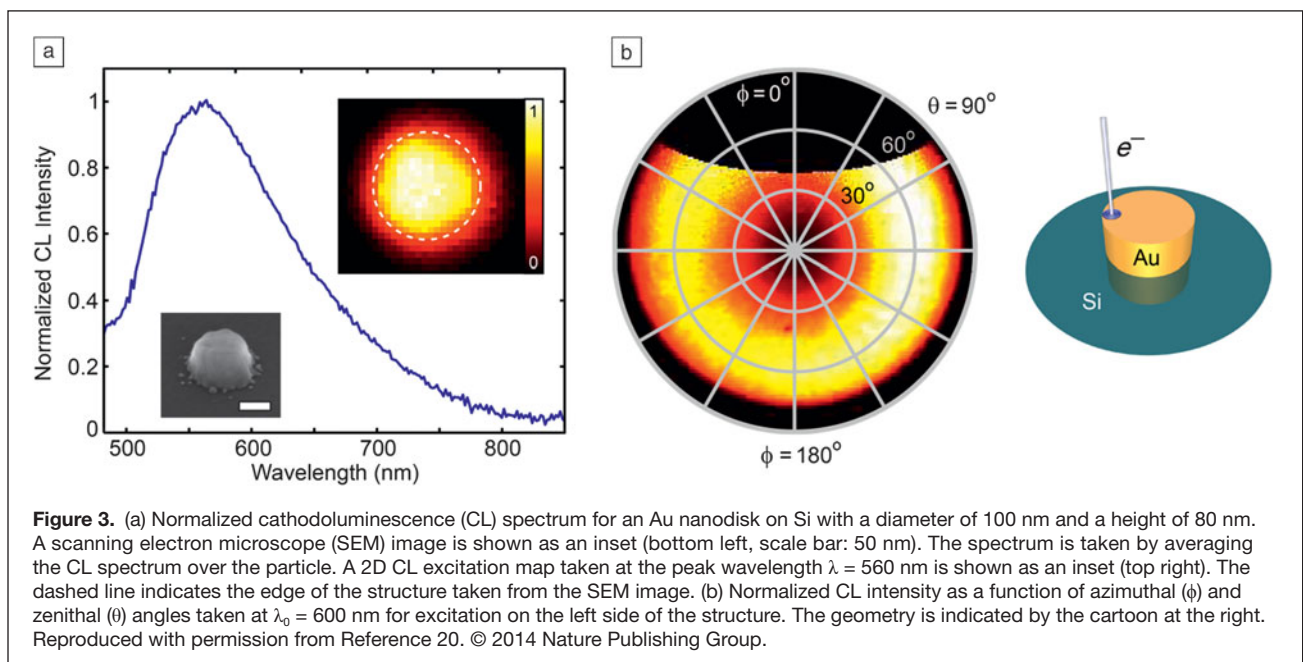


**Figure 4a** shows an SEM image of a 400-nm-deep elliptical cavity, which is sculpted into the surface of a single-crystal gold substrate using focused ion beam milling.<sup>23</sup> These structures serve as cavities for SPPs that propagate at the Au surface and are confined within the cavity walls. The SPP cavity modes are excited with the electron beam, and CL emission is observed due to scattering of SPPs at the cavity walls into the far field. **Figure 4b** shows a 2D spatial excitation map taken at an emission wavelength of  $\lambda_0 = 720$  nm. Two hotspots are observed resulting from the interference of SPPs within the cavity. This modal pattern strongly depends on the size of the SPP wave compared to the cavity size. If the cavity is large compared to the wavelength, higher-order modes are supported and the interference patterns become more complex.<sup>24</sup> An angular emission pattern of the elliptical cavity, which is excited in one of the emission maxima, shows clear directional beaming of light at a wavelength of  $\lambda = 600$  nm (**Figure 4c**).

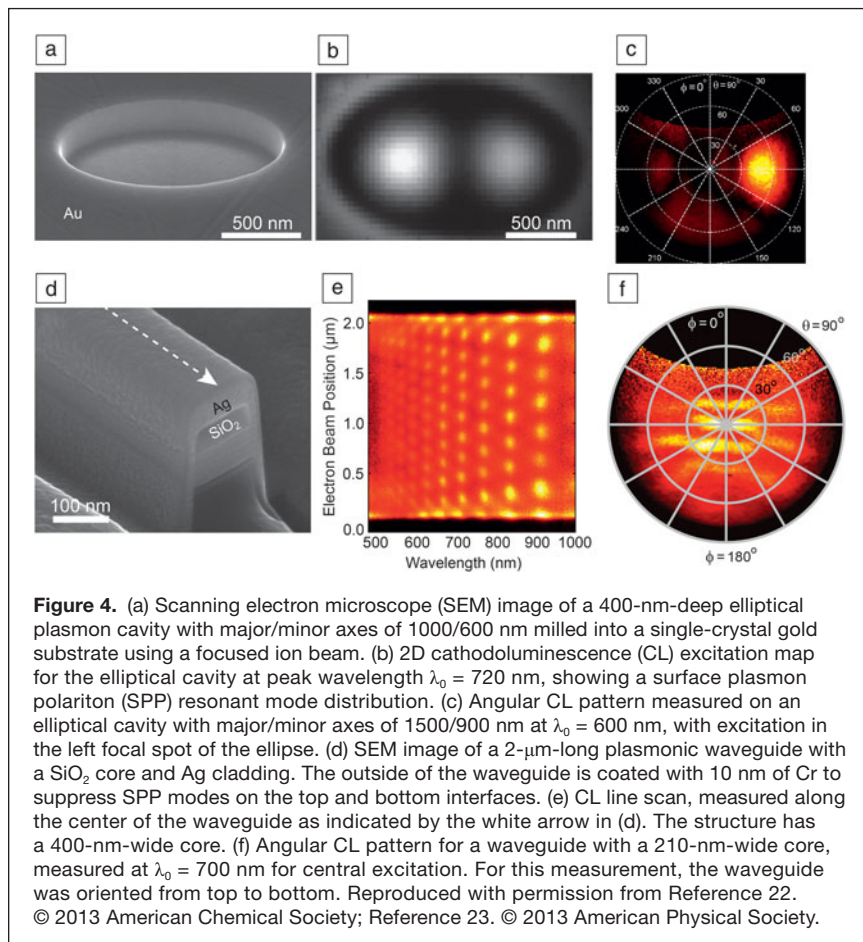
**Figure 4d** shows an SEM image of a linear SPP waveguide composed of a dielectric silica core surrounded by Ag.<sup>25</sup> In such coaxial waveguides, strong coupling occurs between SPPs that propagate at the internal silica/Ag interfaces, and a hybrid SPP mode forms of which the dispersion (the relation between wave vector and frequency) strongly depends on the core dimensions. The silica/Ag waveguide has a length of 2  $\mu\text{m}$ ;

therefore, standing SPP waves will form due to reflection of SPPs at the waveguide outer facets. CL spectra were taken by scanning the electron beam along the central axis of the waveguide (dashed line in **Figure 4d**).

**Figure 4e** shows these standing waves, taken at a broad range of emission wavelengths in the range  $\lambda_0 = 500$ –1000 nm. At each optical frequency, or vacuum wave length, a characteristic standing wave pattern is observed, the period of which is determined by the SPP wavelength at that frequency. SPPs have short wavelengths at frequencies corresponding to a free space wavelength of  $\lambda_0 = 500$  nm and long wavelengths for frequencies corresponding to a wavelength of  $\lambda_0 = 1000$  nm. In this way, the SPP dispersion diagram can be fully reconstructed. In this experiment, light is mostly collected from the two output facets. As the SPPs are coherently excited, there is a well-defined phase relation between these radiating point sources, which leads to a fringe interference pattern in the angular radiation patterns, as can be seen in **Figure 4f**.<sup>25</sup> Nanostructures supporting SPPs find applications in, for example, subwavelength optical components,<sup>26</sup> lasers,<sup>27</sup> LEDs,<sup>28</sup> solar cells,<sup>29</sup> and sensors.<sup>30</sup>

### Excitation of dielectric nanostructures

Imaging and angle-resolved CL is a powerful tool for studying localized and propagating plasmon resonances in metallic nanostructures; however, the concept of coherent electron-beam excitation is generally applicable to any polarizable medium including semiconductors and dielectrics. **Figure 5a** shows an electron micrograph of a silicon disk fabricated by electron-beam lithography in combination with reactive ion etching into the top layer of a silicon-on-insulator substrate.<sup>31</sup> The silicon disk shown in the image has a diameter of 200 nm and a height of 100 nm and is placed on a 300-nm-thick  $\text{SiO}_2$  layer with a thick silicon substrate underneath. These dielectric nanocavities possess Mie-type resonant modes in which the local fields are mostly confined within the Si disk. **Figure 5b** shows a 2D excitation map for a 320-nm-diameter disk at a wavelength of  $\lambda_0 = 475$  nm. A radially symmetric excitation distribution is observed, which reflects the resonant field distribution in the cavity. For this particular example, a minimum is observed in the center, and several subsequent maxima and minima are observed as the electron beam is moved outward. The angular emission pattern of such a structure shows an upward beaming of light within a relatively narrow cone (**Figure 5c**). Dielectric nanostructures can find applications in microcavity lasers,<sup>32</sup> integrated optical components, and light scattering layers in photovoltaics,<sup>33</sup> among others.



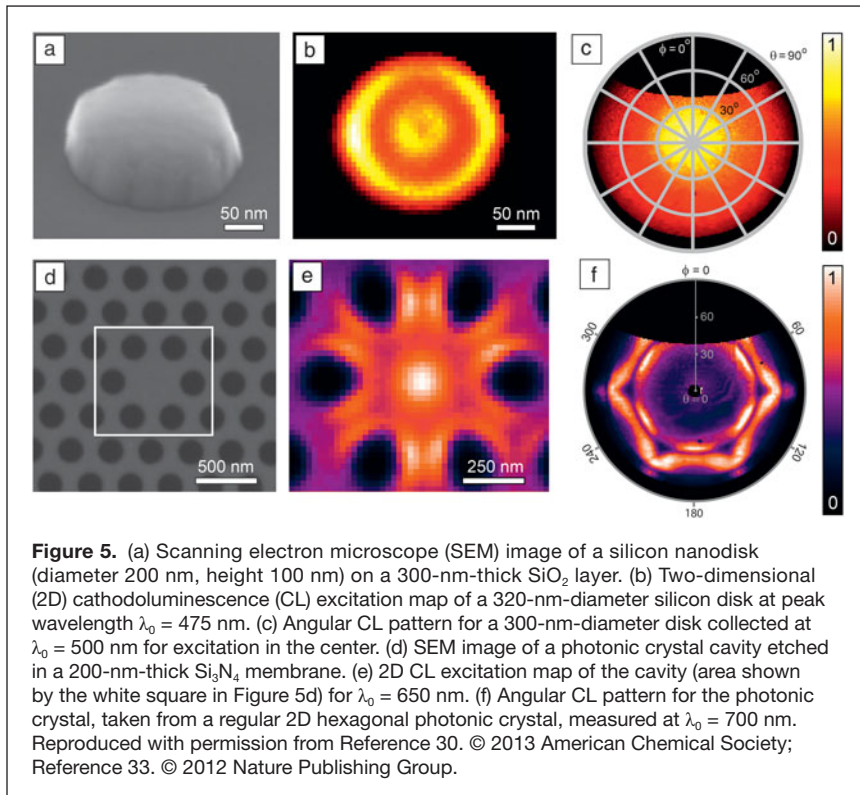


**Figure 5.** (a) Scanning electron microscope (SEM) image of a silicon nanodisk (diameter 200 nm, height 100 nm) on a 300-nm-thick  $\text{SiO}_2$  layer. (b) Two-dimensional (2D) cathodoluminescence (CL) excitation map of a 320-nm-diameter silicon disk at peak wavelength  $\lambda_0 = 475$  nm. (c) Angular CL pattern for a 300-nm-diameter disk collected at  $\lambda_0 = 500$  nm for excitation in the center. (d) SEM image of a photonic crystal cavity etched in a 200-nm-thick  $\text{Si}_3\text{N}_4$  membrane. (e) 2D CL excitation map of the cavity (area shown by the white square in Figure 5d) for  $\lambda_0 = 650$  nm. (f) Angular CL pattern for the photonic crystal, taken from a regular 2D hexagonal photonic crystal, measured at  $\lambda_0 = 700$  nm. Reproduced with permission from Reference 30. © 2013 American Chemical Society; Reference 33. © 2012 Nature Publishing Group.

### Excitation of photonic crystals

The power of the angle-resolved detection capability becomes clear further in CL studies of photonic crystals. Figure 5d shows an electron micrograph of a 200-nm-thick  $\text{Si}_3\text{N}_4$  membrane in which a hexagonal photonic crystal is made using a combination of electron-beam lithography and reactive ion etching.<sup>34</sup> In this particular example, a point defect cavity is created by removing a hole in the center. The photonic crystal is designed such that light propagation in the plane of the crystal is forbidden for a certain wavelength band (the photonic bandgap). In the cavity, however, an optical mode can exist and its field distribution can be directly probed with CL. Figure 5e shows the spatial excitation distribution of the cavity collected at the cavity resonance wavelength of  $\lambda_0 = 650$  nm. A complex field distribution pattern is observed inside the cavity and reveals features at a deep-subwavelength scale. Finally, Figure 5f shows an angular emission pattern from a regular hexagonal photonic crystal (without defect cavity). The hexagonal symmetry of the photonic crystal is clearly reflected in the azimuthal emission distribution. An emission band at a particular zenithal angle is directly related to the wave vector of the mode within the photonic crystal at the corresponding frequency and therefore, such measurements can be used to derive the photonic bandstructure of the photonic crystal in great detail. This analysis can even be performed in a spatially resolved manner, so that the 2D mode profile of each photonic band can be separately mapped. Photonic crystals find applications in, for example, miniature lasers,<sup>35</sup> LEDs,<sup>36</sup> on-chip optical networks and memory,<sup>37</sup> and sensors.<sup>38</sup>

### CL imaging resolution

To first order, the resolution of the coherent CL imaging technique is limited by the spot size of the electron beam, which is typically in the range 1–10 nm, depending on SEM instrument, beam current, and acceleration voltage. The extent of the evanescent electric field about the electron trajectory will determine the spatial range over which a polarizable nanostructure is excited. By carrying out measurements of CL intensity across a square hole made into a thin silicon membrane, we have determined the spatial resolution for 30 keV electron-beam excitation to be 30–40 nm.<sup>34</sup> The field extent can be reduced by lowering the electron energy.

### Summary and outlook

We have developed an angle-resolved CL imaging spectroscopy instrument, which enables excitation and imaging of photonic nanostructures at deep-subwavelength resolution. We used the electron beam as a direct excitation source of polarizable material, creating coherently emitted radiation. In this article, we briefly reviewed our earlier work in this field; more detailed information can be found in the papers that are referenced. We showed how coherent emission can be separated from incoherent emission through angle-resolved measurements. Additionally, resonant plasmonic modes are excited in single metallic nanoparticles, and SPPs are excited at the surface of a metal. By imaging cavity resonant field distributions, we can derive the dispersion of SPPs over a broad spectral range. We also showed how resonant modes in dielectric nanocavities and photonic crystal cavities can be excited, and the dispersion of photonic crystals can be directly mapped.

Several new directions in CL imaging spectroscopy can be envisioned. Extension of the detection wavelength range into the mid-infrared will enable the study of optical phenomena in a wide range of materials, including nanostructured semiconductors and dielectrics, 2D materials such as graphene and boron nitride, and more. By adding time-resolved excitation capabilities, a wealth of new opportunities will emerge in dynamic studies of light in optical nanomaterials. Furthermore, it will be interesting to explore the use of angle-resolved imaging CL in other research and application fields, such as optoelectronic devices, lab-on-a-chip technology, pharmaceuticals, integrated optics, forensics, metallurgy, biophysics, geology, materials science, and metrology. Because of its broad applicability, we expect that CL spectroscopy will play an important role in many scientific developments in the coming years.

### Acknowledgments

This article reviews work carried out in collaboration with Jorik van de Groep, Felipe Bernal Arango, and Femius

Koenderink (AMOLF); David Schoen and Mark Brongersma (Stanford University); Humeyra Caglayan and Nader Engheta (University of Pennsylvania); Javier García de Abajo, Martin Kuttge, Jan Renger, and Niek van Hulst (ICFO, Barcelona); and Riccardo Sapienza (Kings College). Technical support, design, and fabrication from Hans Zeijlemaker, Ilya Cerjak, Wim Brouwer, and Jan van der Linden are gratefully acknowledged. This work is part of the research program of the Foundation for Fundamental Research on Matter (FOM), which is financially supported by the Netherlands Organization for Scientific Research. It is also supported by the European Research Counsel and by NanoNextNL, a research program funded by the Dutch Ministry of Economic Affairs.

## References

1. E. Betzig, J.K. Trautman, *Science* **257**, 189 (1992).
2. T.A. Klar, S.W. Hell, *Opt. Lett.* **24**, 954 (1999).
3. E. Betzig, G.H. Patterson, R. Sougrat, O.W. Lindwasser, S. Olenych, J.S. Bonifacio, M.W. Davidson, J. Lippincott-Schwartz, H.F. Hess, *Science* **313**, 1642 (2006).
4. M. Rust, M. Bates, X. Zhuang, *Nat. Methods* **3**, 793 (2006).
5. F.J. García de Abajo, *Rev. Mod. Phys.* **82**, 209 (2010).
6. B.G. Jacobi, D.B. Holt, *Cathodoluminescence of Inorganic Solids* (Plenum, New York, 1990).
7. A.C. Zonneville, R.F.C. van Tol, N. Liv, A.C. Narvaez, A.P.J. Eftting, P. Kruit, J.P. Hoogenboom, *J. Microsc.* **252**, 58 (2013).
8. F.J. García de Abajo, M. Kociak, *Phys. Rev. Lett.* **100**, 106804 (2008).
9. T. Coenen, E.J.R. Vesseur, A. Polman, *Appl. Phys. Lett.* **99**, 143103 (2011).
10. N. Yamamoto, S. Ohtani, F.J. García de Abajo, *Nano Lett.* **11**, 91 (2011).
11. B.J.M. Brenny, T. Coenen, A. Polman, *J. Appl. Phys.* **115**, 244307 (2014).
12. H. Mertens, J.S. Biteen, H.A. Atwater, A. Polman, *Nano Lett.* **6**, 2622 (2006).
13. K.C.Y. Huang, M.K. Seo, T. Sarmiento, Y. Huo, J.S. Harris, M.L. Brongersma, *Nat. Photonics* **8**, 244 (2014).
14. L. Novotny, N. van Hulst, *Nat. Photonics* **5**, 83 (2011).
15. H.R. Stuart, D.G. Hall, *Appl. Phys. Lett.* **69**, 2327 (1996).
16. K.R. Catchpole, A. Polman, *Appl. Phys. Lett.* **93**, 191113 (2008).
17. C. Ayala-Orozco, C. Urban, M.W. Knight, A.S. Urban, O. Neumann, S.W. Bishnoi, S. Mukherjee, A.M. Goodman, H. Charron, T. Mitchell, M. Shea, R. Roy, S. Nanda, R. Schiff, N.J. Halas, A. Joshi, *ACS Nano* **8**, 6372 (2014).
18. J. van de Groep, P. Spinelli, A. Polman, *Nano Lett.* **12**, 3138 (2012).
19. E.C. Garnett, W. Cai, J.J. Cha, F. Mahmood, S.T. Connor, M.G. Cristoforo, Y. Cui, M.D. McGehee, M.L. Brongersma, *Nat. Mater.* **11**, 241 (2012).
20. T. Coenen, E.J.R. Vesseur, A. Polman, A.F. Koenderink, *Nano Lett.* **11**, 3779 (2011).
21. T. Coenen, F. Bernal Arango, A.F. Koenderink, A. Polman, *Nat. Commun.* **5**, 3250 (2014).
22. T. Coenen, A. Polman, *ACS Nano* **8**, 7350 (2014).
23. D.T. Schoen, T. Coenen, F.J. García de Abajo, M.L. Brongersma, A. Polman, *Nano Lett.* **13**, 188 (2013).
24. E.J.R. Vesseur, T. Coenen, H. Caglayan, N. Engheta, A. Polman, *Phys. Rev. Lett.* **109**, 013902 (2013).
25. T. Coenen, E.J.R. Vesseur, A. Polman, *ACS Nano* **6**, 1742 (2012).
26. E. Verhagen, M. Spasenočić, A. Polman, L. Kuipers, *Phys. Rev. Lett.* **102**, 203904 (2009).
27. R.F. Oulton, V.J. Sorger, T. Zentgraf, R.M. Ma, C. Gladden, L. Dai, G. Bartal, X. Zhang, *Nature* **461**, 629 (2009).
28. K. Okamoto, I. Niki, A. Shvartser, Y. Narukawa, T. Mukai, A. Scherer, *Nat. Mater.* **3**, 601 (2004).
29. H.A. Atwater, A. Polman, *Nat. Mater.* **9**, 205 (2010).
30. C. Wu, A.B. Khanikaev, R. Adato, N. Arju, A.A. Yanik, H. Altug, G. Shvets, *Nat. Mater.* **11**, 69 (2012).
31. T. Coenen, J. van de Groep, A. Polman, *ACS Nano* **7**, 1689 (2013).
32. D.K. Armani, T.J. Kippenberg, S.M. Spillane, K.J. Vahala, *Nature* **421**, 925 (2003).
33. P. Spinelli, M.A. Verschuuren, A. Polman, *Nat. Commun.* **3**, 692 (2012).
34. R. Sapienza, T. Coenen, J. Renger, M. Kuttge, N.F. van Hulst, A. Polman, *Nat. Mater.* **11**, 781 (2012).
35. O. Painter, R.K. Lee, A. Scherer, A. Yariv, J.D. O'Brien, P.D. Dapkus, I. Kim, *Science* **284**, 1819 (1999).
36. J.J. Wierer Jr., A. David, M.M. Megens, *Nat. Photonics* **3**, 163 (2009).
37. E. Kuramochi, K. Nozaki, A. Shinya, K. Takeda, T. Sato, S. Matsuo, H. Taniyama, H. Sumikura, M. Notomi, *Nat. Photonics* **8**, 474 (2014).
38. E. Chow, A. Grot, L.W. Mirkarimi, M. Sigalas, G. Girolami, *Opt. Lett.* **29**, 1093 (2004). □



**Toon Coenen** studied chemistry and physics at Utrecht University and received his PhD degree at the FOM Institute AMOLF in Amsterdam, The Netherlands, in 2014 in Albert Polman's group. He co-developed the cathodoluminescence detection system discussed in this article and used it to investigate the nanoscale optical properties of various metallic and dielectric nanostructures. He now works at Delmic, which has developed a commercial version of the instrument discussed in this article.



**Benjamin J. M. Brenny** studied chemistry and physics at Utrecht University. He is currently a PhD candidate in Albert Polman's group investigating infrared cathodoluminescence (CL) spectroscopy and mapping optical band structures of complex photonic systems using CL.



**Ernst Jan Vesseur** studied physics at Utrecht University and received his PhD degree at the FOM Institute AMOLF in Amsterdam, The Netherlands, in 2011 in Albert Polman's group. He co-developed the CL detection system discussed in this article. He now works at FEI Company.



**Albert Polman** is a scientific group leader at the FOM Institute AMOLF. His research group focuses on light management in new photovoltaic materials, optical metamaterials with properties that do not exist in nature, and the development of the cathodoluminescence system discussed in this article. Polman is co-founder and shareholder of Delmic, which developed a commercial version of the instrument described in this article. He is a professor of photonic materials for photovoltaics at the University of Amsterdam and an MRS Fellow. Polman can be reached by email at polman@amolf.nl.